

Enhanced NIR Radiation-Triggered Hyperthermia by Mitochondrial Targeting

Hyo Sung Jung,^{†,⊥} Jiyoun Han,^{‡,⊥} Jae-Hong Lee,[†] Ji Ha Lee,[§] Jong-Min Choi,^{||} Hee-Seok Kweon,[#] Ji Hye Han,[▽] Jong-Hoon Kim,^{*,‡} Kyung Min Byun,^{*,||} Jong Hwa Jung,^{*,§} Chulhun Kang,^{*,▽} and Jong Seung Kim^{*,†}

[†]Department of Chemistry, Korea University, Seoul 136-701, Korea

[‡]Division of Biotechnology, Laboratory of Stem Cells and Tissue Regeneration, College of Life Sciences and Biotechnology, Korea University, Seoul 136-713, Korea

[§]Department of Chemistry and Research Institute of Natural Science, Gyeongsang National University, Jinju 660-701, Korea

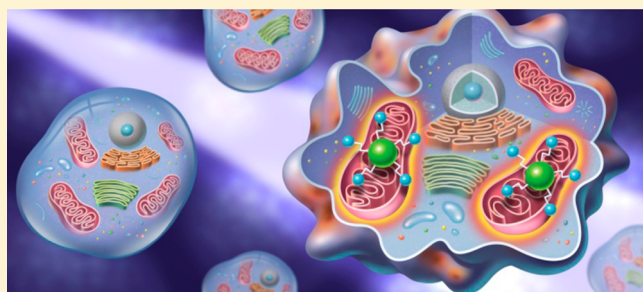
^{||}Department of Biomedical Engineering, Kyung Hee University, Yongin 446-701, Korea

[#]Division of Electron Microscopic Research, Korea Basic Science Institute (KBSI), Daejeon 305-806, Korea

[▽]The Graduate School of East-West Medical Science, Kyung Hee University, Yongin 446-701, Korea

Supporting Information

ABSTRACT: Mitochondria are organelles that are readily susceptible to temperature elevation. We selectively delivered a coumarin-based fluorescent iron oxide nanoparticle, **Mito-CIO**, to the mitochondria. Upon 740 nm laser irradiation, the intracellular temperature of HeLa cells was elevated by 2.1 °C within 5 min when using **Mito-CIO**, and the treatment resulted in better hyperthermia and a more elevated cytotoxicity than HeLa cells treated with coumarin iron oxide (**CIO**), which was missing the mitochondrial targeting unit. We further confirmed these results in a tumor xenograft mouse model. To our knowledge, this is the first report of a near-infrared laser irradiation-induced hyperthermic particle targeted to mitochondria, enhancing the cytotoxicity in cancer cells. Our present work therefore may open a new direction in the development of photothermal therapeutics.



INTRODUCTION

Hyperthermia, a therapeutic procedure to induce apoptosis in tumor tissues, is an efficient complement to standard cancer treatments (radiotherapy and chemotherapy) that artificially elevates tissue temperatures^{1,2} to take advantage of cells with a weak defense against heat, causing minimal side effects.³ Several heat delivery materials, including nanoparticles (NPs), have been developed for applications in anticancer therapy.^{4,5} Many studies have investigated methods to enhance the hyperthermic efficacy of the NPs by varying their size, shape, surface charge, and coating material (e.g., protein, polymer, or cell-penetrating peptides).^{6–11}

Recently, heat-generation systems using near-infrared (NIR) laser irradiation have attracted attention because they are less invasive and less harmful to normal tissues than other methods.^{12,13} Among the NIR-sensitive NPs, magnetic particles (MPs) such as iron oxide particles (IOPs) are excellent candidates for hyperthermic anticancer therapy, because they are nontoxic, biocompatible, and, in addition, compatible with magnetic resonance imaging technology.^{4a,14–16} To achieve higher radiation-to-heat conversion in hyperthermia with the NIR-sensitive MPs, the delivery of large amounts of MPs has

been pursued; however, this method can increase damage to normal cells too.^{17–19} In this study, we demonstrate a novel method to enhance cytotoxicity for a given amount of heat by selectively delivering MPs to a thermally susceptible subcellular organelle with minimal side effects.

Mitochondria are critical energy-producing cellular organelles and are highly sensitive to heat shock,^{20–22} frequently causing apoptotic cell death through the production of reactive oxygen species (ROS).^{23,24} Recently, the synergy of mitochondrial targeting and magnetic field-induced hyperthermia was exploited by Shah et al. to utilize an enhanced effect on mitochondrial dysfunction, resulting in cell apoptosis.²⁵ Therefore, MP delivery to mitochondria may enhance hyperthermic cytotoxicity. Herein, we describe the design and synthesis of mitochondria-targeting iron oxide NPs (Figure 1) composed of a lipophilic triphenylphosphonium cation (TPP) for efficient mitochondrial targeting^{26–29} and a coumarin fluorophore for fluorescence-based real-time tracking of its uptake and distribution into various subcellular compartments. We show

Received: December 2, 2014

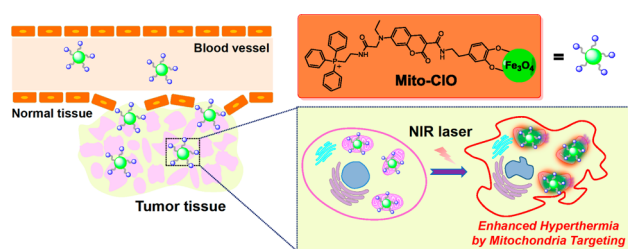


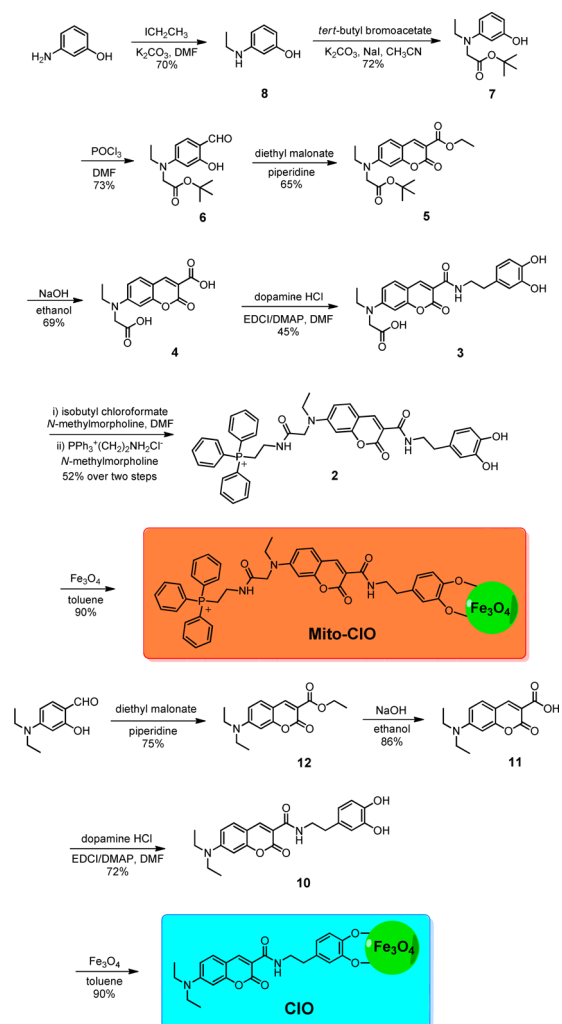
Figure 1. Schematic representation of enhanced hyperthermia by using mitochondria-targeting iron oxide NPs.

that the specially designed NPs localize preferentially to mitochondria and induce significant cell hyperthermia upon NIR irradiation.

RESULTS AND DISCUSSION

Synthesis and Characterization of Coumarin Iron Oxides. Mitochondrial-targeted coumarin iron oxide (**Mito-CIO**) and coumarin iron oxide (**CIO**) were synthesized as outlined in Scheme 1. Coupling of 3-aminophenol and

Scheme 1. Synthetic Routes to Mito-CIO and CIO^a



^aDMF, *N,N*-dimethylformamide; EDCI, 1-ethyl-3-(3-(dimethylamino)propyl)carbodiimide; DMAP, 4-dimethylaminopyridine.

iodoethane in the presence of potassium carbonate (K_2CO_3) in dimethylformamide (DMF) yielded **8**,³⁰ which was further reacted with *tert*-butyl bromoacetate, K_2CO_3 , and potassium iodide to produce **7**. Through a Vilsmeier–Haack reaction, **7** was converted to **6**, which then underwent a piperidine-catalyzed Knoevenagel condensation with diethyl malonate to produce the coumarin derivative **5**. Compound **3** was obtained from **5** via a deprotection with sodium hydroxide in ethanol and the subsequent coupling with dopamine hydrochloride by using 1-ethyl-3-(3-(dimethylamino)propyl)carbodiimide (EDCI) and 4-dimethylaminopyridine (DMAP). Compound **2** was obtained from **3** by reaction with $(PPh_3^+(CH_2)_2NH_2)Cl^-$ in the presence of isobutyl chloroformate in DMF. To demonstrate that the TPP unit in **2** was responsible for mitochondrial targeting,^{26–29} an analogue lacking the TPP unit, **10**, was also prepared as a comparison. Coupling of dopamine hydrochloride with **11**, prepared according to previously reported methods,³¹ yielded compound **10**. The chemical structures of **2** and **10** were confirmed by ¹H NMR, ¹³C NMR, FT-IR, and ESI-MS analyses (see Supporting Information).

To prepare **Mito-CIO** and **CIO**, IOPs were added to an anhydrous toluene solution of compounds **2** or **10**. The mixtures were refluxed with continuous stirring under N_2 atmosphere for 24 h. The collected products were washed three times with dichloromethane and acetone to remove excess **2** or **10** and dried under vacuum. Functionalization of **Mito-CIO** and **CIO** was characterized by transmission electron microscopy (TEM), thermogravimetric analysis (TGA), infrared spectroscopy (IR), and X-ray photoelectron spectroscopy (XPS). TEM images of iron oxide-based **Mito-CIO** revealed spherical particles with a diameter of ~ 15 nm and a narrow size distribution (Figure 2a). Their distinct lattice fringe patterns

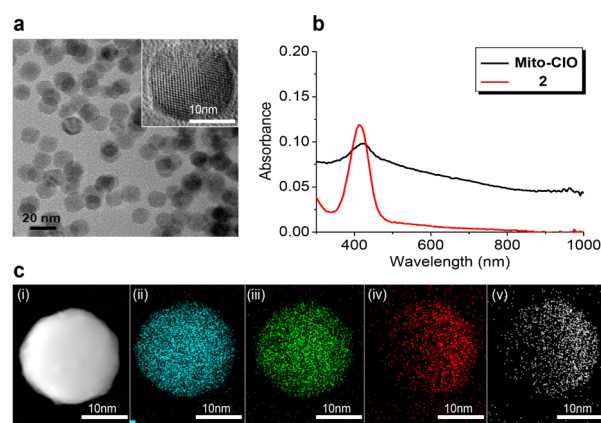


Figure 2. Characterization of **Mito-CIO**. (a) TEM image of **Mito-CIO**. Inset: high-resolution TEM image. (b) UV–vis absorption spectra of **Mito-CIO** and compound **2**. (c) TEM mapping image of **Mito-CIO**: (i) bright-field image, (ii) iron, (iii) oxygen, (iv) nitrogen, and (v) phosphorus components.

were evident in a high-resolution TEM image (Figure 2a, inset), indicative of a highly crystalline nature. The IR spectra of **Mito-CIO** showed strong new bands at 3300, 2922, 2848, 1692, 1614, 1576, 1511, 1432, 1260, 1224, and 1015 cm^{-1} that originated from **2** (Figure S1). The XPS spectrum of **Mito-CIO** (Figure S2) revealed an increase in nitrogen atoms, thereby confirming the presence of **2** on the surface of the iron oxide NPs. **Mito-CIO** is composed of 67.5% carbon, 5.6% nitrogen, 22.7% oxygen, and 4.1% phosphorus, and TEM mapping

results showed that Mito-CIO contains carbon, oxygen, nitrogen, phosphorus, and iron (Figure 2c). These findings confirmed that compound **2** was securely attached to the surface of NPs, accounting for ~52.0 wt % of Mito-CIO as determined by TGA (Figure S3). The reference material (CIO) without the targeting unit was characterized as a comparison (see Supporting Information). Aqueous dispersions of Mito-CIO and CIO displayed a broad and continuous absorption and an increased NIR absorption (Figures 2b and S5b).

Photothermal Conversion Efficiency of Mito-CIO. The photothermal conversion efficiency of Mito-CIO dispersed in a phosphate-buffered saline (PBS, pH 7.4) solution was investigated as a function of concentration and NIR irradiation power. Upon irradiation with a 740 nm NIR laser at 2.0 W/cm², we observed that the temperature of the dispersed solution gradually increased with the concentration (Figure 3a). The

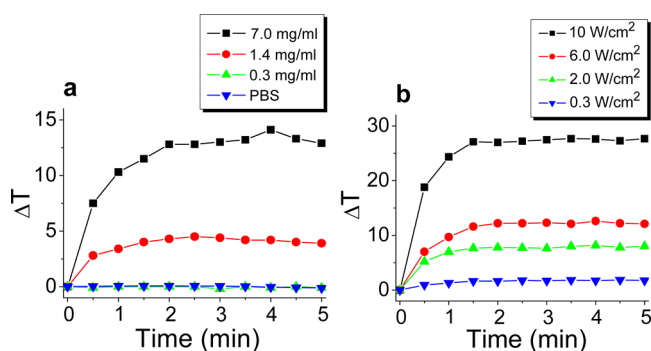


Figure 3. Photothermal conversion efficiency of Mito-CIO. Hyperthermia heating curves of Mito-CIO dispersed in PBS solution (pH 7.4) at (a) various Mito-CIO concentrations (0, 0.3, 1.4, and 7.0 mg/mL) with irradiation at 2.0 W/cm² and (b) 1.4 mg/mL Mito-CIO with irradiation at various intensities (0.3, 2.0, 6.0, and 10 W/cm²) as a function of irradiation time.

solution at 7.0 mg/mL showed a ~13 °C increase in temperature within 2 min, whereas no such change was observed with the particle-free solution. Furthermore, the temperature of the dispersed solution at 1.4 mg/mL markedly increased as the laser power increased from 0.3 to 10 W/cm² (Figure 3b). These results demonstrate that the heat is generated by NIR irradiation of the iron oxide-based Mito-CIO, with an excellent photothermal conversion efficiency.

Photothermal Conversion Efficiency of Mito-CIO Inside HeLa Cells. To characterize the photothermal conversion efficiency of the MPs inside cells, the temperature of HeLa cells loaded with Mito-CIO was monitored under constant NIR irradiation by using an infrared thermal camera (Figure 4a). The local temperature at the irradiation point increased with increasing laser power (Figure 4b,c). In particular, 10 W/cm² irradiation with a 740 nm NIR laser rapidly elevated the temperature of Mito-CIO loaded cells by 2.14 ± 0.25 °C within 5 min, whereas such a change was negligible without Mito-CIO (approximately 0.3 °C). These results demonstrate that Mito-CIO is capable of elevating the cell temperature upon NIR irradiation. We next tested whether this NP-based hyperthermia is sufficient to induce cell death.

Cytotoxicity of CIO-Loaded HeLa Cells. To investigate and fluorescently visualize the cytotoxicity upon NIR irradiation, Mito-CIO- or CIO-loaded HeLa cells were prestained with propidium iodide (PI) and calcein AM. Irradiation of the Mito-CIO-loaded cells reveals a clear

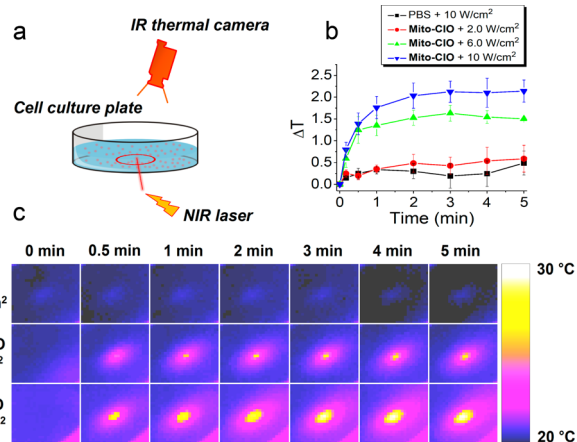


Figure 4. Photothermal conversion efficiency of Mito-CIO inside cells. (a) Schematic diagram of HeLa cells in a delta T dish loaded with Mito-CIO upon NIR laser irradiation. The red circle shows the area of laser illumination. The local temperature change was monitored using an IR thermal camera. (b) Hyperthermia heating curves. (c) IR thermal images of HeLa cell media with and without Mito-CIO at various irradiation intensities (2.0, 6.0, and 10 W/cm²) as a function of irradiation time.

demarcation between the green calcein AM- and red PI-fluorescent regions (Figure 5a), indicating that the irradiation is

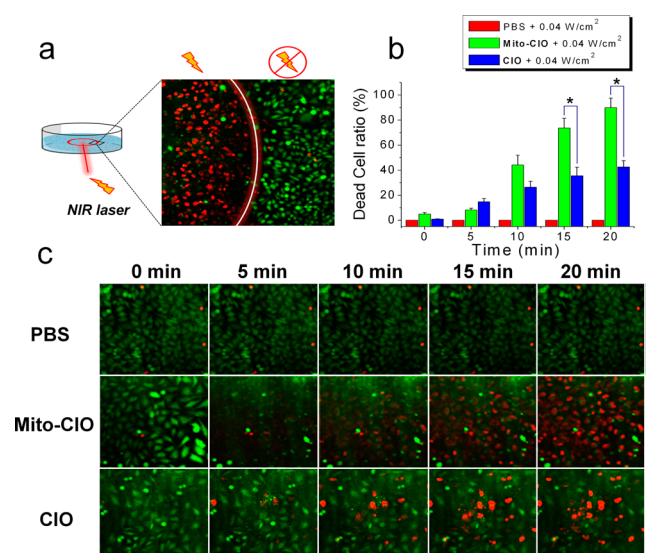


Figure 5. Cytotoxicity of HeLa cells loaded with Mito-CIO and CIO. (a) Confocal fluorescence microscopic images of HeLa cells treated with Mito-CIO following NIR irradiation (740 nm, 0.04 W/cm²) for 20 min. (b) Dead cell ratio (cytotoxicity is defined as a number of PI positive cells of the number of the total cells) and (c) confocal fluorescence microscopic images of HeLa cells treated with PBS, Mito-CIO and CIO following laser irradiation (740 nm, 0.04 W/cm²) for 20 min as a function of irradiation time. Live/dead cells are green/red (Calcein AM/PI), respectively. **P* < 0.05.

indeed a critical factor in cell cytotoxicity as determined by the percentage of PI-stained cells. The fluorescence microscopic results in Figure 5c revealed more rapid and extensive cell death for Mito-CIO than for CIO. The cytotoxicity induced by irradiated Mito-CIO reached $89.90 \pm 7.72\%$ within 20 min, whereas that by CIO was $42.58 \pm 5.09\%$ under similar experimental conditions. Consequently, Mito-CIO showed no

significant cytotoxicity when the cells were not irradiated (Figure S6) but induced the superior cytotoxicity than **CIO** upon NIR irradiation. The fluorescence intensities (FI) of HeLa cells treated with **Mito-CIO** and **CIO** were approximately equal (FI = 14.15 ± 0.18 and 14.98 ± 0.27 , respectively) (Figure S7), indicating that differential amounts of **Mito-CIO** or **CIO** delivered to the cells are not responsible for the superior cytotoxicity of **Mito-CIO**. Moreover, the coumarin moiety in the chemical structure is not responsible for the superior cytotoxicity of **Mito-CIO**, compared to **CIO** (Figure S8). The enhanced cytotoxic effect of **Mito-CIO** could, therefore, be attributed to its TPP moiety, which is a well-known mitochondrial targeting unit and absent in **CIO**. Thus, we propose that the hyperthermic cytotoxicity of **Mito-CIO** may depend on its intracellular localization. The mode of cell death by the hyperthermic cytotoxicity of **Mito-CIO** was examined by using annexin V-fluorescein isothiocyanate (annexin V-FITC) and PI stainings (Figure S9). Before NIR irradiation, neither annexin V-FITC nor PI-stained cells were observed, but at 6 h after NIR laser irradiation, both annexin V-FITC and PI stained cells were observed simultaneously. These results thus indicate that hyperthermic cytotoxicity by the **Mito-CIO** induces mixed types of cell death, necrosis, and apoptosis.

Co-Localization of Mito-CIO and CIO with Fluorescent Organelle Trackers. To identify the intracellular localizations of the **CIOs**, we performed TEM imaging and fluorescence co-localization experiments employing organelle trackers (Mito-, ER-, and LysoTracker Red). The fluorescence localization of **Mito-CIO** overlapped with that of MitoTracker (Pearson's coefficient (PC) 0.871) but only partially overlapped with Lyso- (PC 0.550) or ER-Tracker (PC 0.664) (Figure 6). This strongly indicates that **Mito-CIO** localizes to the mitochondria (Figure 6c). In comparison, **CIO** primarily localized to the ER

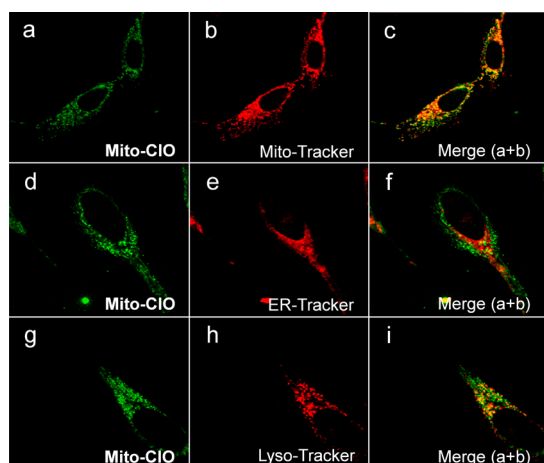


Figure 6. Confocal fluorescence microscopic images of HeLa cells treated with **Mito-CIO** and MitoTracker Red, ER-Tracker Red, or LysoTracker DND-99. (a, d, and g) Fluorescent images of **Mito-CIO** in HeLa cells excited at 740 nm (two-photon excitation) and collected at 450–550 nm. (b) Fluorescent image of MitoTracker Red (0.2 μM) collected using a 650–700 nm filter with excitation at 633 nm. (c) Merged image of (a) and (b). PC: 0.871. (e) Fluorescent image of ER-Tracker Red (0.5 μM) collected using a 600–650 nm filter with excitation at 543 nm (two-photon excitation). (f) Merged image of (d) and (e). PC: 0.550. (h) Fluorescent image of LysoTracker DND-99 (0.5 μM) collected using 600–650 nm filter with excitation at 543 nm (two-photon excitation). (i) Merged image of (g) and (h). PC: 0.664.

(PC 0.833) (Figure S10). We further confirmed the mitochondrial localization of **Mito-CIO** by TEM (Figure S11), revealing that the dark iron oxide particles, which were identified by their diameters, are located in the mitochondria. These results confirm that the TPP unit of **Mito-CIO** causes preferential localization to the mitochondria.^{26–29} Therefore, intracellular hyperthermia induced by NIR-sensitive **CIOs** in the mitochondria exerts cytotoxic effects superior to **CIOs** in other subcellular locations.

In Vivo Xenografted Tumor Imaging and Therapy by Using MPs.

To gain insight into the cytotoxicity of **CIOs** in an animal model, we examined the *in vivo* tumor target specificity and therapeutic potential of **Mito-CIO** in A549 cell xenografted BALB/c nude mice. The A549 cells are human adenocarcinomic alveolar basal epithelial cells, which reported a relatively slow vascular formation in a xenograft mouse model.³² Generally, fast growing tumor vasculature in immunocompromised mouse models can be a bias for evaluating tumor targeting efficiency. Therefore, to avoid this undesirable bias, we used A549 cells as our xenograft model. We intravenously injected mice tails with either PBS (control group) or **Mito-CIO** and observed gradually increased fluorescence signals in the **Mito-CIO** group. The maximum signal intensity at the tumor site was observed 6 h after injection, confirming that **Mito-CIO** can target tumors *in vivo* (Figure 7a). Examination of the *ex vivo* fluorescence biodistribution revealed that **Mito-CIO** and **CIO** preferentially accumulated at the tumor site (>10-fold higher than the normal liver, kidney, heart, lung, and spleen tissues; $P < 0.05$) (Figure 7b,c). We measured the tumor levels of **CIOs** by inductively coupled plasma atomic emission spectroscopy (ICP-AES) and found that the amount of accumulated iron in the tumor tissues (w/w) was similar among the **IO**, **Mito-CIO** and **CIO**-injected groups (8.288 ± 0.919 , 11.2552 ± 1.774 , and 8.939 ± 0.982 , respectively ($\times 10^{-5}$)) (Figure 7d). However, the iron was not detectable in the tumor tissues of the control group ($P < 0.05$, compared to all **CIO**-injected groups). Accumulation of NPs inside tumors is assumed to be mediated by an enhanced permeability and retention effect.^{33,34}

We examined the therapeutic effects of **IO**, **Mito-CIO**, and **CIO** upon NIR irradiation in the tumor xenograft model (Figure 7e). After six doses with NIR irradiation on one side of the grafted tumor region, the irradiated tumor volume in the **Mito-CIO** group was significantly reduced compared to the nonirradiated tumor volume (Figure 7f, $P < 0.05$). In particular, the **Mito-CIO** treatment induced a more dramatic decrease in the tumor volume after day 28 (Figure 7g). Histochemical analysis revealed several regions of increased cell death in the tumor tissue of the **Mito-CIO**-injected group after photothermal therapy (Figure 7h, inside area of black dashes in lower left panel) compared to the PBS control group. Furthermore, proliferating cell nuclear antigen (PCNA) staining of tumor cryosections also showed that proliferation was significantly decreased in the **Mito-CIO**-treated group, and Prussian blue staining detected increased iron in the tumor from the **Mito-CIO**-treated group, compared to the PBS group (Figure 7h).

Considering the similar amounts of accumulated iron oxide localized to the tumor sites (Figure 7d), the superior antitumor efficacy of **Mito-CIO** may be attributed to its TPP moiety. The agreement between the therapeutic effects of **CIOs** in the animal model and the *in vitro* cytotoxicity results (Figure 5) suggests that mitochondria-directed photothermal therapy may be a more effective cancer treatment.

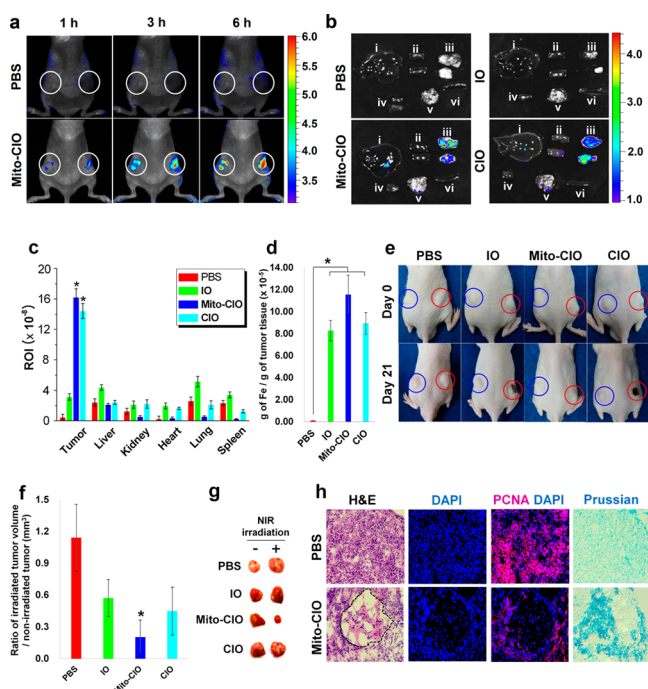


Figure 7. *In vivo* xenograft tumor imaging and therapy using MPs. (a) *In vivo* NIR image of xenografted BALB/c nude mice 1, 3, and 6 h after tail intravenous injection of PBS or Mito-CIO. (b) *Ex vivo* fluorescence in various tissues (i: liver, ii: kidney, iii: tumor, iv: heart, v: lung, and vi: spleen) from xenografted BALB/c nude mice 6 h after injection with PBS, IO, Mito-CIO, or CIO. (c) Quantification of *ex vivo* fluorescence [regions of interest (ROI) as individual pixels]. (d) Quantification of accumulated iron in tumor tissues by ICP-AES. (e) Representative images of xenografted BALB/c nude mice on day 0 and 21 days after 740 nm photothermal therapy of the right tumor (red circle). The left tumor (blue circle) was used as nonirradiated control. (f) Ratio of irradiated tumor volume to nonirradiated tumor volume. * $P < 0.05$. (g) Dissected tumor tissues from each group after photothermal therapy. (h) Histochemical analysis of snap-frozen tumor cryosection from PBS and Mito-CIO mice after photothermal therapy. Photothermal cell death is indicated by the black dashed area in the H&E-stained panel. PCNA with DAPI staining indicates cellular proliferation. Prussian blue indicates intracellular iron accumulation. Magnification: 200 \times .

CONCLUSIONS

We prepared a new mitochondria-targeting iron oxide NP fabricated with two functional groups: TPP as the mitochondrial targeting unit and coumarin as a fluorescent signaling unit. Upon irradiation with a 740 nm NIR laser at 2.0 W/cm², the solution temperature of Mito-CIO was increased by 13 °C, whereas no such changes occurred in a NP-free solution. Laser irradiation of HeLa cells incorporating Mito-CIO increased the cellular temperature by 2.1 °C within 5 min. In HeLa cells, Mito-CIO and CIO were localized to the mitochondria and the ER, respectively. Mito-CIO induced significantly more cell death after 20 min NIR irradiation than did CIO, and the differential cytotoxicity can be attributed to the mitochondrial localization of NPs. Furthermore, *in vivo* therapy using mitochondria-directed hyperthermia clearly displayed tumor suppression, which is in agreement with the *in vitro* cytotoxicity results. Together, these results strongly support our hypothesis that mitochondria are more susceptible to hyperthermia than the ER. From this study of both the *in vitro* and *in vivo* effects of mitochondria-targeted MPs, we conclude that this heat

generating system can enhance the therapeutic efficacy of hyperthermia in cancer treatment and may allow the development of new photothermal therapeutics.

EXPERIMENTAL SECTION

Synthetic Materials and Methods. UV–vis and ESI-MS spectra were obtained using Shinco S-3100 spectrophotometers and Shimadzu LCMS-2020, respectively. NMR spectra were collected on either Varian 300 or Varian 400 MHz spectrometers. IR spectra were recorded on a Shimadzu FTIR 8400S instrument. TEM images of the NPs were taken on a JEOL JEM-2010 transmission electron microscope operating at 200 kV (293 K) using an accelerating voltage of 100 kV and a 16 mm working distance. XPS analysis of the NPs was measured by XPS (X-ray photoelectron spectroscopy, Sigma Probe, Thermo-VG, England) with monochromatic Al K α (1486.7 eV) X-ray source. TGA data were obtained with the TA Instruments Q-50.

Synthesis of Iron Oxide NPs. These NPs were synthesized by the previously reported procedure.³⁵ A mixture of iron(III) chloride hexahydrate (5.4 g, 20 mmol) and sodium oleate (18.3 g, 60 mmol) in a solvent mixture (40 mL EtOH, 30 mL distilled water and 70 mL hexane) was stirred at 70 °C. After a 4 h reaction, the organic layer was washed with distilled water, and the organic layer was collected. After removal of the solvents, the iron–oleate complex was obtained as a solid. For preparation of the monodisperse iron oxide NPs (12 nm), oleic acid (2.9 g, 10 mmol) and 1-octadecene (100 g) were added to the iron–oleate complex (18.0 g, 20 mmol) at 25 °C, and the solution was stirred at 320 °C and maintained constant heating rate (3.3 °C min⁻¹). After 30 min reaction, the reaction mixture including the NPs was cooled to 25 °C, and the precipitates were washed with ethanol (200 mL \times 3) to remove the excess oleate. The NPs were prepared by separation using a centrifuge.

Cell Culture and Confocal Microscopy Study. HeLa cells were cultured in DMEM (Invitrogen) applied with 10% FCS (Invitrogen). The cells were seeded onto 24-well flat-bottomed plates 1 day prior to the confocal imaging experiments. After 1 day later, Mito-CIO (1.40 mg/mL) and CIO (1.22 mg/mL) were added to the cells to confirm their cellular localization and cytotoxicity as mentioned in this manuscript. To check cellular localization of CIOs, the cells were pretreated with media containing organelle trackers (Mito- (0.2 μ M), Lyso- (0.5 μ M), and ER (0.5 μ M) tracker, respectively, Invitrogen) prior to incubation for 2 h with CIOs and washed with PBS buffer three times. HeLa cells incubated with organelle trackers and CIOs were measured by a Leica TCS-SP2 confocal fluorescence multiphoton microscope. For monitoring cell cytotoxicities, propidium iodide (PI, 50 μ g/mL in PBS buffer, Aldrich) and calcein AM (1 μ g/mL in PBS buffer, Aldrich) were used. The HeLa cells were incubated 2 h with or without CIOs prior to incubation with media containing PI and calcein AM and then subjected to the 740 nm pulsed laser exposure (1.3 mW, 200 fs, 90 MHz) with 0.04 W/cm² power densities for 20 min. The cytotoxicity results in HeLa cells were monitored under a Leica TCS-SP2 confocal fluorescence multiphoton microscope.

MTT Assay. HeLa Cells were washed with 1 mL of PBS twice and the medium was changed into FBS-free DMEM culture media prior to assay. The cell viability was tested by the MTT (3-(4,5-dimethylthiazol-2-yl)-2,5 diphenyltetrazolium bromide, Life Technologies, Carlsbad, CA, USA) assay following the manufacturer's instruction. Briefly, HeLa cells (1.5×10^4 cells in 100 μ L of media) were seeded onto a 96-well plate. On the following day, the culture medium was changed, and cells were incubated with different concentrations (0.70, 1.40, 7.00, 14.0, 21.0, or 28.0 mg/mL) of CIOs in 100 μ L of fresh medium at 37 °C for 6 h. After 6 h, the medium was discarded, and prepared culture medium containing 12 mM MTT solution was added into each well, including a negative control of culture media alone. After 1 h incubation, the medium was removed from the wells. Then 30 μ L of DMSO was added to each well and mixed thoroughly for 15 min. The supernatant of each well was transferred to a 96-well plate, and the absorbance was measured at 540 nm using a microplate spectrophotometer (PowerWave XS, Bio-Tek, Winooski, VT, USA).

Monitoring the Mode of Cell Death by the Hyperthermic Cytotoxicity of Mito-CIO. HeLa cells (2.0×10^6 per dish) were seeded on 35 mm confocal dishes (glass bottom dish, SPL, Kyong-Gi, Republic of Korea) and stabilized for 48 h. Then the cells were treated with 1.40 mg/mL Mito-CIO in 2 mL culture medium. After 2 h incubation, the cells were irradiated with a 740 nm pulsed laser (0.04 W/cm² power densities) for 10 min to induce hyperthermic cytotoxicity. Six h later, the mode of cell death was examined by using an annexin V-FITC and PI staining kit according to manufacturer's instructions (BD, San Jose, California, USA). The results in HeLa cells were monitored under a confocal fluorescence microscope.

Photothermal Conversion Efficacy. To investigate the photo-thermal conversion effect, a series of solutions of Mito-CIO (0, 0.3, 1.4, and 7.0 mg/mL, respectively) in pH 7.4 PBS solution were irradiated by the 740 nm pulsed laser exposure (1.3 mW, 200 fs, 90 MHz) with 2.0 W/cm² power densities during 5 min. To verify the function of NIR laser power density, the solutions of Mito-CIO (1.4 mg/mL) in pH 7.4 PBS were irradiated with different NIR power densities (0.3, 2.0, 6.0, and 10 W/cm²). The temperature changes were measured with an IR thermal camera (A300, FLIR, Boston, MA) over 5 min. The camera captured a time series of images that display solution temperatures by color. All the experiments were conducted at room temperature.

In Vitro Photothermal Conversion Efficacy. HeLa cells were incubated with Mito-CIO (1.4 mg/mL) and then subjected to the 740 nm pulsed laser exposure (1.3 mW, 200 fs, 90 MHz) with different power densities (0.3, 2.0, 6.0, and 10 W/cm²) over 5 min. During exposure to a NIR laser, thermographic images were recorded with a FLIR thermal camera at a time interval of 10 s over a course of 5 min, and the temperature of the HeLa cells was calculated from the data using FLIR R&D software. All the experiments were conducted at room temperature.

Bio-TEM Image. The HeLa cells were grown on the MatTek Petri dish with CELLocate coverslips and incubated for 2 h with Mito-CIO (1.40 mg/mL) and washed with PBS buffer three times. Mito-tracker Red (0.2 μ M) was used for mitochondrial staining. Imaging was done with a Leica TCS-SP2 confocal fluorescence multiphoton microscope. After this observation, the cells were then fixed with 2.5% glutaraldehyde (pH 7.3, 0.1 M phosphate buffer) at 25 °C for 1 h. Then, the cells were treated with 1% OsO₄ plus 1.5% potassium ferrocyanide (pH 7.3, 0.1 M phosphate buffer) at 4 °C in the dark for 1 h and embedded in Epon 812 after dehydration with an ethanol and propylene oxide series. After 2 days polymerization at 70 °C with pure resin, 70 nm ultrathin sections were collected with an ultramicrotome (UltraCut-UCT, Leica, Austria). Then, the sections were collected on copper grids (100-mesh). After staining (2% uranyl acetate (15 min) and lead citrate (5 min)), bio-TEM images of the sections were taken on a JEOL JEM-1400Plus transmission electron microscopy operating at 120 kV.

The Retention of the Iron Oxide NPs Inside the Tumor Tissues. The tumor-bearing mice were tail-intravenously injected with PBS, 3.36 mg/mL IO, 7.00 mg/mL Mito-CIO, and 7.47 mg/mL CIO in 70 μ L PBS. After 6 h, the injected mice were terminated. The tumor tissues (0.1 g) were dissected and immersed in 0.5 mL of water. The immersions were ground into a mash with a tissue grinder, and 0.5 g of aqua regia was added. After 10 days, the tissue samples were centrifuged, the supernatants were collected and diluted with 9 mL of water. The concentrations of iron in these solutions were measured in triplicate by ICP-AES (Perkin-Elmer Optima 4300 DV, USA) at the Korean Basic Science Institute (KBSI). The calculated average iron concentration as determined from three independent samples.

Mouse Xenograft Model. To examine the therapeutic effect and imaging of Mito-CIO and CIO in the tumor tissue, 6- to 8-week-old BALB/c nude mice were purchased from RaonBio (Kayonggido, Yonginsu, South Korea) (control xenograft, $n = 8$; treatment injected xenograft, $n = 8$). All animals were acclimatized to the animal facility for at least 48 h prior to experimentation and maintained according to the Guide for the Care and Use of Laboratory Animals published by the NIH. They were housed in a barrier under HEPA filtration and

provided with sterilized food and water *ad libitum*. Animal facility was kept 12 h light/dark cycles at room temperature 21 ± 2 °C with 30–40% humidity. Approximately 5.0×10^6 cells of A549 were mixed with 354234-matrigel (BD) and subcutaneously injected in the right and left flanks.

In and Ex Vivo Imaging. *In vivo* and *ex vivo* investigations were examined to evaluate the tumor target specificity and organ distribution of CIOs using A549 inoculated xenograft mice. After 4–5 weeks of inoculation, xenograft mice were assigned into four groups, and tail intravenous injection of 3.36 mg/mL IO, 7.00 mg/mL Mito-CIO, and 7.47 mg/mL CIO in 70 μ L PBS was performed. As a negative control, 70 μ L PBS was injected. After tail intravenous injection, *in vivo* spectral fluorescence images were measured by using an *in vivo* imaging system (IVIS) spectrum (PerkinElmer, Waltham, MA, USA). For *ex vivo* images, the tumor tissues and other organs (lung, heart, liver, kidney, and spleen) of all animals were dissected 6 h after injection with PBS, IO, Mito-CIO, or CIO and observed by using an IVIS spectrum. The filter set for both *in vivo* and *ex vivo* images was Blue: excitation and emission; 430 to 500 nm. The fluorescence images consisting of spectra and autofluorescence were then unmixed with commercial software (Living Image software for IVIS Spectrum/200, ver. 4.1, Waltham, MA, USA).

In Vivo Therapy. To validate the therapeutic effect, the initiated tumor volume and size were weekly measured with a digital caliper. CIOs were tail intravenously injected 6 times every other day as described above. Six h after injection, 740 nm pulsed laser irradiation (1.3 mW, 200 fs, 90 MHz) with 2.0 W/cm² power densities for 10 min was performed on the tumors on the right side in each of the xenograft mice of the four different groups. Then final tumor volume, size, and weight on both sides were measured at 3 weeks subsequent to the last injection and irradiation treatment.

Histochemistry Analysis. After taking *ex vivo* images, the grafted tumor tissues and other organs (lung, heart, liver, kidney, and spleen) were dissected and embedded in Tissue-Tek 100% optimal cutting temperature compound (O.C.T., Sakura Finetek, USA) for cryosection. Then the fresh tissue was rapidly snap frozen by placing it into liquid nitrogen, and the tissues were stored in a –80 °C freezer until further analysis. Freshly cryopreserved tissues were cut (6 μ m thick) using a –25 °C ultramicrotome (Leica CM 3050 S, Wetzlar, Germany). Each section was picked up on an adhesion microscope glass slide (Paul Mariendeld GmbH & Co.KG, Lauda-Königshofen, Germany), and then the O.C.T compound was carefully washed out with PBS (twice). The tissue cryosections were stained with hematoxylin (Merck, Readington Township, NJ, USA) and eosin (H&E) (BBC Biochemical, Mt. Venom, WA, USA).

For PCNA immunohistochemistry of tumor cryosection, snap frozen tumor sections were washed with PBS and blocked with 10% goat or donkey serum in PBS. Then, the tissue sections were incubated for 24 h at 4 °C with anti-PCNA antibodies (Abcam, Cambridge, MA, USA) diluted with 10% goat or donkey serum in PBS. On the following day, the tissue sections were washed with PBS and incubated at room temperature for 1 h with appropriate secondary antibodies (Life Technologies, Carlsbad, CA, USA). Nuclei were labeled with 4,6-diamidino-2-phenylindole (DAPI; Sigma-Aldrich, St. Louis, MO, USA) for 5 min. After rinsing in 70% ethanol for 5 min, tissue sections were treated with an autofluorescence eliminator reagent (Millipore, Billerica, MA, USA) for 5 min to avoid false positive signals. Finally, tissue sections were washed and mounted with Immumount (Thermo, Waltham, MA, USA) and examined with an Axiovert 200 M fluorescence microscope (Zeiss, Oberkochen, Germany).

■ ASSOCIATED CONTENT

📄 Supporting Information

Synthesis, structural characterization, subcellular localization, functional characterization of NPs, and biological evaluations. This material is available free of charge via the Internet at <http://pubs.acs.org>.

AUTHOR INFORMATION

Corresponding Authors

*jhkim@korea.ac.kr

*kmbyun@khu.ac.kr

*jonghwa@gnu.ac.kr

*kangch@khu.ac.kr

*jongskim@korea.ac.kr

Author Contributions

[†]These authors contributed equally.

Funding

The authors declare no competing financial interest.

Notes

The authors declare no competing financial interest.

ACKNOWLEDGMENTS

This work was supported by CRI project (no. 2009-0081566 to J.S.K.), Basic Science Research Program (2012R1A1A2006259 to C.K.) from the National Research Foundation of the Ministry of Science, ICT & Future Planning in Korea, the Next-Generation BioGreen 21 Program (SSAC) (PJ009041022012 to J.H.J) from the Rural development Administration in Korea, and the National Research Foundation of Korea (NRF) grant funded by the Korea government (MEST) (NSF-2013R1A1A1A05011990 to K.M.B.) and the National Research Foundation of Korea (NRF) grant funded by the Korea government (MEST) (no. 2012M3A9B4028636 to J.-H.K.).

REFERENCES

- (1) Dickson, J. A.; Calderwood, S. K. In *Hyperthermia in Cancer Therapy*; Storm, F. K., Ed.; G. K. Hall Medical Publishers: Boston, MA, 1983; pp 63–140.
- (2) Hildebrandt, B.; Wust, P.; Ahlers, O.; Dieing, A.; Sreenivasa, G.; Kerner, T.; Felix, R.; Riess, H. *Crit. Rev. Oncol. Hematol.* **2002**, *43*, 33–56.
- (3) Urano, M.; Duple, E. B. In *Hyperthermia and oncology. Vol 1. Thermal effects on cells and tissues*; VSP: Utrecht, 1988.
- (4) (a) Lim, E.-K.; Kim, T.; Paik, S.; Haam, S.; Huh, Y.-M.; Lee, K. *Chem. Rev.* **2015**, *115*, 327–394. (b) Choi, W. I.; Kim, J.-Y.; Kang, C.; Byeon, C. C.; Kim, Y. H.; Tae, G. *ACS Nano* **2011**, *5*, 1995–2003.
- (5) Robinson, J. T.; Tabakman, S. M.; Liang, Y.; Wang, H.; Casalogue, H. S.; Vinh, D.; Dai, H. *J. Am. Chem. Soc.* **2011**, *133*, 6825–6831.
- (6) Yin, Y.; Alivisatos, A. P. *Nature* **2005**, *437*, 664–670.
- (7) Lundqvist, M.; Stigler, J.; Elia, G.; Lynch, I.; Cedervall, T.; Dawson, K. A. *Proc. Natl. Acad. Sci. U.S.A.* **2008**, *105*, 14265–14270.
- (8) Bartczak, D.; Muskens, O. L.; Nitti, S.; Sanchez-Elsner, T.; Millar, T. M.; Kanaras, A. G. *Small* **2012**, *8*, 122–130.
- (9) Yang, H. W.; Hua, M. Y.; Liu, H. L.; Tsai, R. Y.; Chuang, C. K.; Chu, P. C.; Wu, P. Y.; Chang, Y. H.; Chuang, H. C.; Yu, K. J.; Pang, S. T. *ACS Nano* **2012**, *6*, 1795–1805.
- (10) Yuan, H.; Fales, A. M.; Vo-Dinh, T. *J. Am. Chem. Soc.* **2012**, *134*, 11358–11361.
- (11) Ahmadi, T. S.; Wang, Z. L.; Green, T. C.; Henglein, A.; El-Sayed, M. A. *Science* **1996**, *272*, 1924–1925.
- (12) O'Neal, D. P.; Hirsch, L. R.; Halas, N. J.; Payne, J. D.; West, J. L. *Cancer Lett.* **2004**, *209*, 171–176.
- (13) Melancon, M. P.; Zhou, M.; Li, C. *Acc. Chem. Res.* **2011**, *44*, 947–956.
- (14) Yu, T. J.; Li, P. H.; Tseng, T. W.; Chen, Y. C. *Nanomedicine* **2011**, *6*, 1353–1363.
- (15) Liao, M. Y.; Lai, P. S.; Yu, H. P.; Lin, H. P.; Huang, C. C. *Chem. Commun.* **2012**, *48*, 5319–5321.
- (16) Colombo, M.; Carregal-Romero, S.; Casula, M. F.; Gutiérrez, L.; Morales, M. P.; Böhm, I. B.; Heverhagen, J. T.; Prosperi, D.; Parak, W. *J. Chem. Soc. Rev.* **2012**, *41*, 4306–4334.
- (17) Cherukuri, P.; Glazer, E. S.; Curley, S. A. *Adv. Drug Delivery Rev.* **2010**, *62*, 339–345.
- (18) Laurent, S.; Mahmoudi, M. *Int. J. Mol. Epidemiol. Genet.* **2011**, *2*, 367–390.
- (19) Wang, Y.; Wang, K.; Zhao, J.; Liu, X.; Bu, J.; Yan, X.; Huang, R. *J. Am. Chem. Soc.* **2013**, *135*, 4799–4804.
- (20) Flanagan, S. W.; Moseley, P. L.; Buettner, G. R. *FEBS Lett.* **1998**, *431*, 285–286.
- (21) Zuo, L.; Christofi, F. L.; Wright, V. P.; Liu, C. Y.; Merola, A. J.; Berliner, L. J.; Clanton, T. L. *Am. J. Physiol. Cell. Physiol.* **2000**, *279*, C1058–C1066.
- (22) Willis, W. T.; Jackman, M. R.; Bizeau, M. E.; Pagliassotti, M. J.; Hazel, J. R. *Am. J. Physiol. Regul. Integr. Comp. Physiol.* **2000**, *278*, R1240–R1246.
- (23) Yuen, W. F.; Fung, K. P.; Lee, C. Y.; Choy, Y. M.; Kong, S. K.; Ko, S.; Kwok, T. T. *Life Sci.* **2000**, *67*, 725–732.
- (24) Wang, Z.; Cai, F.; Chen, X.; Luo, M.; Hu, L.; Lu, Y. *PLoS One* **2013**, *8*, e75044.
- (25) Shah, B. P.; Pasquale, N.; De, G.; Tan, T.; Ma, J.; Lee, K.-B. *ACS Nano* **2014**, *8*, 9379–9387.
- (26) Chen, X.; Tian, X.; Shin, I.; Yoon, J. *Chem. Soc. Rev.* **2011**, *40*, 4783–4804.
- (27) (a) Pan, Y.; Leifert, A.; Ruau, D.; Neuss, S.; Bornemann, J.; Schmid, G.; Brandau, W.; Simon, U.; Jahnen-Dechent, W. *Small* **2009**, *5*, 2067–2076. (b) Pathak, R. K.; Kolishetti, N.; Dhar, S. *Wiley Interdiscip. Rev.: Nanomed. Nanobiotechnol.* DOI: 10.1002/wnan.1305.
- (28) Bae, S. K.; Heo, C. H.; Choi, D. J.; Sen, D.; Cho, E. H.; Cho, B. R.; Kim, H. M. *J. Am. Chem. Soc.* **2013**, *135*, 9915–9923.
- (29) Masanta, G.; Lim, C. S.; Kim, H. J.; Han, J. H.; Kim, H. M.; Cho, B. R. *J. Am. Chem. Soc.* **2011**, *133*, 5698–5700.
- (30) Yang, Z.; He, Y.; Lee, J.-H.; Park, N.; Suh, M.; Chae, W.-S.; Cao, J.; Peng, X.; Jung, H. S.; Kang, C.; Kim, J. S. *J. Am. Chem. Soc.* **2013**, *135*, 9181–9185.
- (31) Jung, H. S.; Kwon, P. S.; Lee, J. W.; Kim, J. I.; Hong, C. S.; Kim, J. W.; Yan, S.; Lee, J. Y.; Lee, J. H.; Joo, T.; Kim, J. S. *J. Am. Chem. Soc.* **2009**, *131*, 2008–2012.
- (32) Cascone, T.; Herynk, M. H.; Xu, L.; Du, Z.; Kadara, H.; Nilsson, M. B.; Oborn, C. J.; Park, Y.-Y.; Erez, B.; Jacoby, J. J.; Lee, J.-S.; Lin, H. Y.; Ciardiello, F.; Herbst, R. S.; Langley, R. R.; Heymach, J. V. *J. Clin. Invest.* **2011**, *121*, 1313–1328.
- (33) Maeda, H. *Bioconjugate Chem.* **2010**, *21*, 797–802.
- (34) Iyer, A. K.; Khaled, G.; Fang, J.; Maeda, H. *Drug Discovery Today* **2006**, *11*, 812–818.
- (35) Park, J.; An, K.; Hwang, Y.; Park, J.-G.; Noh, H.-J.; Kim, J.-Y.; Park, J.-H.; Hwang, N.-M.; Hyeon, T. *Nat. Mater.* **2004**, *3*, 891–895.